

# Journal of Materials Chemistry C

Accepted Manuscript



This is an *Accepted Manuscript*, which has been through the Royal Society of Chemistry peer review process and has been accepted for publication.

*Accepted Manuscripts* are published online shortly after acceptance, before technical editing, formatting and proof reading. Using this free service, authors can make their results available to the community, in citable form, before we publish the edited article. We will replace this *Accepted Manuscript* with the edited and formatted *Advance Article* as soon as it is available.

You can find more information about *Accepted Manuscripts* in the [Information for Authors](#).

Please note that technical editing may introduce minor changes to the text and/or graphics, which may alter content. The journal's standard [Terms & Conditions](#) and the [Ethical guidelines](#) still apply. In no event shall the Royal Society of Chemistry be held responsible for any errors or omissions in this *Accepted Manuscript* or any consequences arising from the use of any information it contains.

# BN-Decorated Graphene Nanoflakes for Tunable Opto-electronic and Charge Transport Properties

Cite this: DOI: 10.1039/x0xx00000x

Somananda Sanyal,<sup>a</sup> Arun K. Manna<sup>a</sup> and Swapan K. Pati<sup>a,b,\*</sup>,

Received 00th January 2012,  
Accepted 00th January 2012

DOI: 10.1039/x0xx00000x

[www.rsc.org/](http://www.rsc.org/)

Electronic structures, optical and charge transport properties of various boron-nitrogen (BN) substituted hexagonal graphene nanoflakes (h-GNFs) are investigated aiming to tailor the intrinsic properties of pristine h-GNFs, using first-principles density functional theory. We consider coronene as the smallest h-GNF and compare the structure-property responses with its iso-electronic BN analogues. Three BN analogues of pristine coronene, namely mid-BN-coronene (middle hexagonal ring CC bonds are substituted by BN), peri-BN-coronene (all peripheral CC bonds are substituted by BN) and full-BN-coronene (all CC bonds are replaced by BN) are considered. The results show tunable opto-electronic properties depending on BN concentrations and its position. The study also considers examining the effects of BN concentrations on the opto-electronic properties of larger sized h-GNFs. In addition, we find that the bulk electronic and charge transport (carriers' mobility's) properties of different BN analogues of coronene strongly depends on the nature of BN substitution, with increasing electron mobility found with increase in BN concentrations. We provide microscopic understanding for the tunable properties by analyzing certain intrinsic quantities, such as, extent of orbital delocalization, electronic gap, electrostatic potential, reorganization energy, charge transfer integrals, density of states, etc. The study suggests that optoelectronic and charge transport properties can be tailored through appropriate tuning of BN contents in h-GNFs, thereby paving the way for designing advanced optoelectronic devices.

**Keywords:** Coronene and its iso-electronic BN analogues, Electronic structure, Optical property, Charge transport, Mobility, DFT

## 1. Introduction:

Development and rational designing of organic thin-film transistors (OTFTs)<sup>1</sup> have been the subject of interest in recent times. The acceptance of organic semiconductors on a broad spectrum hinges on the development of materials with high quality process-ability leading to less expensive designing and fabrication. To understand the correlation between solid-state ordering and electronic performance, commercialization of xerography had intensified, where the differences in efficiency of carrier production and charge carrier mobility was found to be associated to differences in aggregate interactions.

Along these lines, both experimentalists and theoreticians have focused to understand the structure-property relationship of various emerging materials, for the opto-electronic properties.<sup>2-8</sup> Very recently studies on the excited electronic states and optical absorption characteristics of coronene, hexa-*peri*-hexabenzocoronene (HBC), and circumcoronene have been done using symmetry-adapted cluster-configuration interaction (SAC-CI) method.<sup>9</sup> In addition, graphene electronics

or photonics is an emerging field of interest in recent times because of its high optical transmittance over a broad spectrum range (both visible and IR) besides its remarkably high carrier mobility.<sup>10, 11</sup>

Substitutions of carbon (C) with boron (B) and nitrogen (N), neighbours of C in the periodic table, in PAHs and their functionalized derivatives, have attracted attention for quite some time now.<sup>12</sup> B-N being isoelectronic and isosteric with C-C, having strong similarity to graphite, substitution of the C-C units in the known PAHs does not alter the structural features, but brings about substantial changes in the chemical properties. The electronic structure of PAHs can be tuned to efficiency by substitutions along the peripheral regions. These molecular systems find wide applications in the field of nano-electronics<sup>13, 14</sup>, optical devices, colorimetric sensors<sup>15, 16</sup>, field emission, catalysis and lubrication. Charge transfer characteristic too is found to change depending on the substitution positions, giving varied applications in molecular electronic devices as purely hole-transporters.

Planar PAHs too have been studied extensively because of the presence of extended  $\pi$ -conjugation in these systems.<sup>17, 18</sup> Coronene (with  $D_{6h}$  symmetry) can be considered as the smallest unit of a graphene nanoflake (GNF), with the dangling bonds saturated with hydrogen atoms, and so, substituting coronene molecule with B-N pairs gives fascinating results in terms of their electronic and photophysical properties, retaining their structural features finding wide applications in optoelectronic devices.<sup>19-25</sup> Synthesis of B-N pyrene, where the  $\pi$ -stacking over herringbone arrangement is favoured, in solid state<sup>26</sup> with internalized B-N moieties, and subsequent theoretical studies on the aromatic nature of it have also been reported.<sup>27</sup> Besides, metal doped systems have also been studied to reflect the fact that electronic and optical properties get altered on substitution/doping.<sup>28</sup> To mention here, a single crystal of coronene, synthesized experimentally<sup>29, 30</sup>, was also studied theoretically to understand their electronic and charge carrier' properties.<sup>31-32</sup>

GNF, a zero-dimensional dot (quantum dot), can also be considered a little bigger form of coronene molecule, where the number of fused benzene rings increase in both directions to form either zig-zag edged or arm-chair edged GNF. From synthetic point of view, these are prepared by bottom-up approach with desired size, structure and symmetry properties.<sup>33</sup> It is important to understand the properties of these structures as they have potential applications in the field of spintronics and optical nanodevices.<sup>34</sup> The size ranges from molecular to semi-infinite 2D forms and so the electronic structures also vary from having molecular levels to band-like, with increasing dimensions. The optical characteristics of GNFs can be attuned by functionalization, which opens up the possibility of using them in optoelectronic devices.<sup>35</sup>

Theoretical studies, mostly using Density Functional Theory (DFT), have been carried out extensively, to realize the changes in the properties of substituted systems. For example, effect of domain segregation<sup>36</sup>, aromatic property changes<sup>37</sup>, hydrogen chemisorption to nitrogen doped coronene molecule<sup>38</sup>, replacement of CH moieties in acenes by nitrogen atoms for studying effect on electron affinities, excitation<sup>39</sup>, cage aromaticity and reactivity of  $B_{12}N_{12}$  clusters with H-doping<sup>40</sup> and first principles study of oxidation of 2D hexagonal boron nitride (h-BN) monolayer<sup>41</sup> to name a few.

In this study, we have studied a few BN substituted h-GNFs, namely, fully BN substituted coronene (full-BN-coronene) and two partially BN substituted coronene, where all carbon atoms of central hexagonal ring are substituted by BN (mid-BN-coronene) and all peripheral CC bonds are replaced by BN (peri-BN-coronene). The electronic, photophysical and charge transfer characteristics of these BN substituted h-GNFs are explored in great detail and the obtained results are compared with that found for the pristine analogue, i.e., without any substitution (coronene). We also present a systematic study for understanding the effects of varying sizes of these BN substituted h-GNFs on the calculated properties. Additionally, we compare and contrast the results obtained for their respective bulk electronic and charge transport properties.

## 2. Computational Details:

All the quantum chemical calculations in this work are performed using DFT, as implemented in Gaussian-09<sup>42</sup> software package. We have used B3LYP<sup>43, 44</sup> hybrid functional for all calculations involving the monomers and the dispersion corrected non-local functional,  $\omega$ B97XD, is employed for the geometry optimizations of the dimers for accounting of the dispersion interactions. All geometry optimizations are carried out using the basis set 6-31+g(d,p), at the ground state, with neutral charge and singlet electronic state configuration. The geometries are confirmed to be at local minimum energy structures by analysing the vibrational frequencies. We have done the periodic calculations for investigating bulk electronic properties using the dispersion-corrected GGA/PBE+D (dispersion) density functional employing an extended plane wave basis code, VASP.<sup>45, 46</sup> The charge transfer integrals or hopping matrix elements, site energies and spatial orbital overlap are calculated by fragment orbital method, using the Amsterdam Density Functional (ADF) program.<sup>47</sup> For all ADF calculations, we have used Generalized Gradient Approximation (GGA) within Perdew-Burke-Ernzerhof (PBE)<sup>48</sup> as exchange and correlation functional, and a large triple zeta ( $\zeta$ ) with double polarization (TZ2P) basis set for all atoms. Working formulae and additional details can be found in the Supporting Information.

## 3. Results and discussion:

### 3.1 Structural Stability and Ground State Electronic Structures

Before we discuss the electronic structures of all systems in detail, we begin with analyzing the structural stability of all monomers and dimers considered in the present study. To compare the stability of all four systems, we calculate the binding energy and formation energy of individual monomer. In this work, we have studied a few B-N modified coronene systems of varying substituent concentrations and its position, namely pristine coronene, mid-BN-coronene, peri-BN-coronene and full-BN-coronene, as defined earlier. Optimized structures of four monomers and dimers along with the important bond lengths obtained using dispersion corrected  $\omega$ B97X-D density functional are shown in Fig. 1.

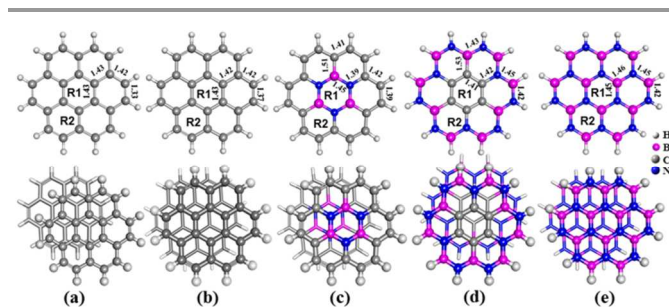


**Figure1:** Optimized geometries of all four monomers (top panel) and dimers (bottom panel) of crystal coronene (a), DFT-optimized coronene (b), mid-BN-coronene (c), peri-BN-coronene (d), and full-BN-coronene (e).

The binding energy ( $E_b^m$ ) per atom of each monomer system is computed using the following formula:

$$E_b^m = [E_{tot} - (\sum N_i E_i)] / N \quad (1)$$

where  $E_{tot}$  = total energy of the system,  $N_i$  = number of  $i^{th}$  element,  $E_i$  = total energy of  $i^{th}$  atom,  $N$  = total number of atoms present in each system. All energies are calculated at the same level of theory.

**Table 1.** Calculated binding energy ( $E_b$ ), formation energy ( $E_f$ ), NICS values, and HOMO (H)-LUMO (L) ( $\Delta E_{H-L}$ ) gap of all monomers.

System	$E_b^m$ (eV/atom)	$E_f$ (eV/atom)	$\Delta E_{H-L}$ (eV)	Ring Num bers	NICS(0)	NICS(1)	NICS(1) <sub>zz</sub>
coronene	-6.87	-6.87	4.02	R1	-0.46	-4.42	-7.62
				R2	-9.98	-11.99	-31.11
mid-BN-coronene	-6.60	-6.41	3.28	R1	-9.24	-10.32	-25.21
				R2	-13.10	-14.19	-38.60
peri-BN-coronene	-6.19	-5.61	5.26	R1	-7.49	-8.93	-21.29
				R2	0.42	-1.55	0.55
full-BN-coronene	-6.09	-5.31	6.64	R1	-0.23	-1.13	3.65
				R2	-0.33	-1.31	1.62

Note that, the way binding energy is defined, provides a measure of cohesive strength of individual system. Large negative  $E_b$  indicates strong cohesive strength and thereby, results in higher structural stability. The results show that the pristine coronene has large negative binding energy (-6.87 eV) and thus is more stable, while its full BN analogue shows less negative binding energy (-6.09 eV), reflecting its less structural rigidity (see Table 1). Two other BN analogues (mid-BN-coronene and peri-BN-coronene) show intermediate binding energies; with slightly more cohesive strength (i.e., more negative binding energy) is found for mid-BN-coronene (see Table 1). We find that larger the number of carbon atoms present within a system, causes more negative binding energy and thus, results in greater structural stability (see Table 1). Note that, pristine coronene has maximum C content and shows large structural stability because of  $\pi$ -electrons delocalization effects. While full-BN-coronene (no C content) is stabilized by charge transfer induced  $p_\pi$ - $p_\pi$  effects. The system's stability arising out of  $\pi$ -electrons delocalization is more compared to the stability gained by charge transfer induced delocalization. Thus, as expected, the results show the following trend in structural stability: pristine coronene > mid-BN-coronene > peri-BN-coronene > full-BN-coronene.

Next, to compare and contrast the formation feasibility of the systems studied, we analyze the formation energy ( $E_f$ ) which is calculated using the following expression:

$$E_f = E_b + n * \Delta\mu_{BN-CC} \quad (2)$$

where  $\Delta\mu_{BN-CC} = \mu_{BN} - \mu_{CC}$ , is the chemical potential difference required for substituting a CC pair by BN pair, and 'n' represents number of each such pair present in BN modified coronene.  $\mu_{BN}$  and  $\mu_{CC}$  are considered to be the binding energy (cohesive energy) per atom per BN and CC pair calculated for their respective pristine molecule, i.e., for coronene and full-BN-coronene, respectively. The difference in chemical potential ( $\Delta\mu_{BN-CC}$ ) is found to be 0.065 eV/atom per BN pair substitution.

Note here that, the definition of formation energy (equation 2) relates the energy cost of forming the BN modified coronene systems from the pristine one. Thus, the formation energy of pristine coronene is equal to its binding energy as there is no substituted BN pair (n=0, see Table 1) and it decreases with increase in BN concentrations. The results show that, the formation energy obtained for the mid-BN-coronene (-6.41 eV/atom) and peri-BN-coronene (-5.61 eV/atom) lies in between that of pristine coronene (-6.87 eV/atom) and full-BN-coronene (-5.31 eV/atom). This clearly suggests the intermediate formation feasibility of these partially BN substituted coronene systems. We also find that, the mid-BN-coronene shows greater formation feasibility than the peri-BN-coronene because of the least number of BN pairs. It is interesting to note that, the formation energy does not vary linearly with the BN concentrations. This is because of the presence of different interfacial energy cost associated with different BN topology present in modified coronene analogues. These results are in good accordance with the thermodynamic formation feasibility of hexagonal  $B_xN_y$  nanodomains hybridized with pristine graphene sheet studied recently.<sup>36</sup>

We now focus on understanding the structural stability of each system by analyzing the local aromaticity descriptor, i.e., NICS (Nucleus Independent Chemical Shift) values calculated at different ring centres. It is found that substitution of coronene all C atoms with B and N, either partially or fully, alters the local aromatic nature of the systems considerably (see Table 1). It is more important to examine the NICS(1) and its zz-component NICS(1)<sub>zz</sub> calculated at 1 Å above the planar ring than NICS(0) which is calculated at the basal plane of the ring considered. It is found that the central ring (R1) of coronene is much more aromatic (large negative NICS) compared to its all B-N substituted analogue. Contrastingly, the central ring (R1) of mid-BN-coronene and peri-BN-coronene shows much more aromatic character than pristine coronene with slightly greater NICS value found for the mid-BN-coronene. The calculated NICS(1) for benzene and borazine<sup>49</sup> are found to be -10.25 and -2.78, respectively, calculated using the same level of theory. These values are very close to the NICS(1) values obtained for coronene and full-BN-coronene calculated at the peripheral ring

center. The NICS(1)zz values calculated at the peripheral ring center (R2) of pristine coronene and mid-BN-coronene shows similar trend, reflecting strong aromatic nature, whereas the values obtained for the mid-BN-coronene and full-BN-coronene suggest anti-aromatic nature (see Table 1). It is interesting to note that, the NICS(1)zz at R2 for mid-BN-coronene is more negative than that found for the pristine coronene. This clearly indicates enhancement in peripheral ring aromaticity for mid-BN-coronene due to the presence of hetero h-BN ring center. It was earlier shown by Rafael *et al.* that borazine can be described as a  $\pi$ -aromatic species, but is not a “globally aromatic” one because of its lesser delocalized nature compared to benzene.<sup>50</sup> High accumulation of electron density on the nitrogen atoms in these systems precludes the overall delocalization of  $\pi$ -electrons through B-atoms, which accounts for the difference in aromatic nature of all these systems. NICS $_{\pi}$  does not account for the  $\sigma$ -contribution but includes the current effects induced by magnetic fields parallel to the ring.<sup>51</sup> Also, presence of any heteroatom in a system affects the topological aromaticity.<sup>27</sup> Another point to focus is that the NICS(0) value of peripheral ring (R2) of peri-BN-coronene is anti-aromatic unlike others. For mid-BN-coronene and full-BN-coronene, the NICS(1) values indicate that R2 is more aromatic compared to R1, while the reverse holds true for peri-BN-coronene, for obvious reasons. Where the central ring is all-C, the delocalization of  $\pi$ -electrons is complete over the central ring. In full-BN-coronene, 7 hexagonal BN rings are fused together, which results in lower aromaticity consistent with decreasing NICS value and expected least delocalization among the B and N atoms. Additionally, we emphasize that the trend in binding energy (i.e., structural stability) is fully consistent with the concept of topological aromaticity.<sup>52</sup>

The intrinsic ground state electronic structure of these systems depends on the nature of BN substitution. We look at the energy gap ( $\Delta E_{H-L}$ ) between the highest occupied molecular orbital (HOMO) and lowest unoccupied molecular orbital (LUMO). The trend in electronic gap follows the order as: full-BN-coronene > peri-BN-coronene > coronene > mid-BN-coronene. Note that, changes in  $\Delta E_{H-L}$  due to BN substitution in coronene imply different extent of HOMO and LUMO molecular orbitals distribution. This strongly governs the photochemical reactivity of the molecule. The FMOs diagram (Fig. 2) shows the HOMO and LUMO are delocalized over the entire molecule, except for the full-BN-coronene where the LUMO is fully localized at the edge atoms. This is in accordance to its highest HOMO-LUMO gap. Interestingly, the results predict least electronic gap for the mid-BN-coronene due to the larger extent of orbital delocalization at the peripheral rings.

Next we discuss the stability of the dimer structures formed from these four coronene monomers. In order to assess the energetic stability of each dimer, we have considered the AB slip-stacked geometry for all four molecules modeled from the pristine coronene crystal structure.<sup>29</sup> For all dimer structures, we have considered full geometry relaxations without any imposed constraint using dispersion corrected hybrid density

functional ( $\omega$ B97XD). The stability of individual stacked dimer is defined by the dimer binding energy ( $E_b^d$ ) and is calculated using the following equation:

$$E_b^d = E_{dimer} - 2 * E_{monomer} \quad (3)$$

where,  $E_{dimer}$  and  $E_{monomer}$  denote the optimized total energy of dimer and monomer using the same dispersion corrected functional  $\omega$ B97XD. The binding energy thus calculated is corrected for the Basis Set Superposition Error (BSSE) using counterpoise method<sup>53, 54</sup>. In Table 2, we provide the inter-planar stacking distance and the binding energy found for each optimized dimer structures. All four optimized dimer geometries are also shown in Fig. 1 (bottom panel).

As given in Table 2, the results show that BN substitution enhances the stability of the dimer compounds (indicative from the relative binding energy values) in comparison to the pristine one. For comparison purpose, we also calculate the binding energy for the pristine coronene dimer structure at the crystallographic geometry. Note that, large negative binding energy suggests greater energetic stability of the stacked dimer structure. In fact, the  $E_b^d$  calculated for the coronene crystal dimer is very large (less negative) than the value obtained for the DFT optimized dimer structure. Also, the inter-planar stacking distance becomes little smaller than that found in isolated crystal coronene dimer upon structural optimization using  $\omega$ B97XD functional. This infers slight underestimation of stacking distances, resulting in large negative binding energy and thereby, imposes strong dimer stability. We should mention that, the stacking distance and binding energy are calculated for an isolated DFT optimized dimer structure, which are compared with the dimer structure present within a crystal environment. This may also cause the differences in stacking distance and binding energy between the two. However, we emphasize that, the comparison of stacking distances and binding energy of individual dimer structure are carried out for their respective isolated DFT optimized geometries using  $\omega$ B97XD density functional. This would provide more appropriate assessment for comparing the energetic stability of the dimer systems investigated here.

From the optimized dimer geometries, the inter-planar distance is found to be 3.45 Å, 3.36 Å, 3.34 Å and 3.25 Å for the pristine coronene, mid-BN-coronene, peri-BN-coronene and full-BN-coronene, respectively. Thus, we find the least stacking distance for the full BN substituted coronene analogue and the distance increases with decreasing BN content. Small stacking distances also causes large binding stability (more negative  $E_b^d$ ) and the dimer stability follows the order of BN concentration. It is interesting to note from all the dimer optimized structures of BN analogues, that the B/N of one plane situates exactly on top of N/B from the another plane due to the intrinsic nature of AB stacked geometry. This causes electrostatic stabilizing interactions between the two layers as the partial positively polarized N atoms of one plane finds negatively polarized B atom of the adjacent plane. This clearly explains the order of binding energy calculated and thereby, the order of dimer

stability. The nature of partial charge distribution is clear from the electrostatic potential (ESP) diagrams (Figure S1). As can be seen, we find similarity in electrostatic potential for coronene and mid-BN-coronene, where the negatively charged  $\pi$ -cloud is found to be delocalized along the ring peripheral region. On the other hand, the ESP calculated for the full-BN-coronene and peri-BN-coronene shows different behavior. These two monomers possess  $\pi$ -electrons clouds that are mostly localized. Moreover, as it is known, partially oppositely polarized B and N atoms take part in electrostatic interactions, while the C atoms from two different planes cause  $\pi$ - $\pi$  orbital interactions.<sup>55</sup>

Apart from the electrostatic stabilization, the formation of these stacked structures is largely governed by the dispersion interactions within the reduced length scale (i.e., small inter-planar separation). To quantify the extent of dispersion interactions (D) acting on each stacked dimer, we calculate D using the binding energy differences obtained with ( $\omega$ B97XD) and without ( $\omega$ B97X) dispersion corrected density functional. The amount of dispersion interactions are given in Table 2. The results show that larger the BN content greater is the dispersion interactions. Thus, we find the following order of D: pristine coronene < mid-BN-cronene < peri-BN-coronene < full-BN-coronene. It is worth to mention that, both electrostatic and dispersion interactions are governing factors for stabilizing these stacked dimer structures. Also, as expected the attractive electrostatic interactions dominate for the dimer stacks of full-BN-coronene and peri-BN-coronene while the repulsive interactions among like negative charges in case of pristine coronene and its topologically similar mid-BN-coronene analogue is more dominant.

**Table 2.** Inter-planar equilibrium distance ( $R_{eq}$ ), binding energy ( $E_b$ ) with and without BSSE corrections, and calculated dispersion energy (D). The electronic HOMO-LUMO gap ( $\Delta E_{H-L}$ ) is also listed.

Systems	$R_{eq}$ (Å)	$E_b^d$ (kcal mol <sup>-1</sup> )	$E_b^d+BSSE$ (kcal mol <sup>-1</sup> )	D (kcal mol <sup>-1</sup> )	$\Delta E_{H-L}$ (eV)
Coronene (Crystal)	3.50	-7.42	-4.88	-13.6	3.78
Coronene (DFT)	3.45	-27.19	-24.08	-15.0	3.77
Mid-BN- coronene	3.36	-28.57	-25.77	-16.8	3.07
Peri-BN- coronene	3.34	-31.27	-28.45	-19.6	5.04
Full-BN- coronene	3.25	-34.12	-30.96	-21.4	6.29

Next, we focus on analysing the ground state electronic properties of these stacked dimer structures and compare with the results obtained for their corresponding monomer. To understand the ground state electronic structure, we calculate the electronic HOMO-LUMO gap ( $\Delta E_{H-L}$ ) and nature of FMOs

distribution. The  $\Delta E_{H-L}$  computed for all these four dimers are provided in Table 2 and the iso-surfaces of HOMO and LUMO are shown in Fig. 4. The results show slightly reduced electronic gap ( $\Delta E_{H-L}$ ) than the values found for the monomer structure. This is because of greater extent of orbital hybridization in the stacked dimer geometries (see Fig. 3) compared to the monomer's FMOs distribution.

### 3.1.2. Optical Absorption of Monomers and Dimers of Coronene and its BN analogues

To gain deeper insight on the optical absorption characteristics of the molecules under study, we have carried out TDDFT calculations, as implemented in Gaussian 09 package, using B3LYP/6-31+g(d,p) level of theory, for analysing the excited state properties. Here we consider the excitation energies of coronene and the three B-N substituted systems with varying BN concentration. Coronene has possible use in scintillation in the blue region of the visible spectrum when illuminated by ultra-violet light. The main transitions that we found for pristine coronene corroborate with the results reported by Fukuda *et al.* using SAC-CI method.<sup>9</sup> Similar to the case of other PAHs, the low-lying ultraviolet-visible (UV-Vis) absorptions of coronene are characterized by three types of valence  $\pi$ - $\pi^*$  transitions, namely  $\alpha$ -,  $p$ -, and  $\beta$ -bands. These correlate with the electronic transitions between two highest occupied molecular orbitals and two lowest unoccupied molecular orbitals. In terms of group theory, the nature of these electronic transitions is similar to that of the valence  $\pi$ - $\pi^*$  transitions in benzene. We find that there is a large hypsochromic shift of absorption wavelength when going from coronene (301.68 nm) to full-BN-coronene (199.33 nm) (see Table 3), while an increase in wavelength is found for mid-BN-coronene, which shows absorption spectra at 344.30 nm, and a little shift towards lower wavelength range is found for peri-BN-coronene (245.31 nm), thereby bringing in the same concept of topological similarity to full-BN-coronene. Obviously, higher the transition energy (lower the absorption wavelength), larger is the energy gap for each system. The red-shifted optical absorption found for mid-BN-coronene is rationalized by the greater extent of  $\pi$ -electrons delocalization at the peripheral C rings. This is also consistent with lowering of electronic gap for this system among other analogues.

**Table 3.** Transition energy, Oscillator strength, significant FMOs contributions for low-energy excitations and energy gap between HOMO and LUMO ( $\Delta E_{H-L}$ ).

Systems	Transition Energy (eV)	Oscillator Strength (f)	OMO $\rightarrow$ UMO (contributions)	$\Delta E_{H-L}$ (eV)
<b>Monomers</b>				
coronene	4.11	0.69	H-1 $\rightarrow$ L (0.39)	4.02
			H $\rightarrow$ L+1 (0.39)	
	4.11	0.69	H-1 $\rightarrow$ L+1 (0.40)	3.28
			H $\rightarrow$ L (0.39)	
mid-BN-coronene	3.60	0.89	H-1 $\rightarrow$ L+1 (0.50)	3.28
			H $\rightarrow$ L (0.50)	
	3.60	0.89	H-1 $\rightarrow$ L (0.50)	5.26
			H $\rightarrow$ L+1 (0.50)	
peri-BN-coronene	5.05	0.63	H-1 $\rightarrow$ L+1 (0.49)	5.26
			H $\rightarrow$ L (0.48)	
	5.05	0.63	H-1 $\rightarrow$ L (0.49)	6.64
			H $\rightarrow$ L+4 (0.41)	
full-BN-coronene	6.22	0.16	H-1 $\rightarrow$ L+3 (0.41)	6.64
			H $\rightarrow$ L+4 (0.41)	
	6.22	0.16	H-1 $\rightarrow$ L+4 (0.41)	6.29
			H $\rightarrow$ L+5 (0.41)	
<b>Dimers</b>				
coronene	4.21	0.68	H-3 $\rightarrow$ L+1 (0.33)	3.77
mid-BN-coronene	3.75	1.20	H-3 $\rightarrow$ L+3 (0.40)	3.07
peri-BN-coronene	5.13	0.46	H $\rightarrow$ L+7 (0.25)	5.04
full-BN-coronene	6.44	0.12	H-1 $\rightarrow$ L+9 (0.46)	6.29

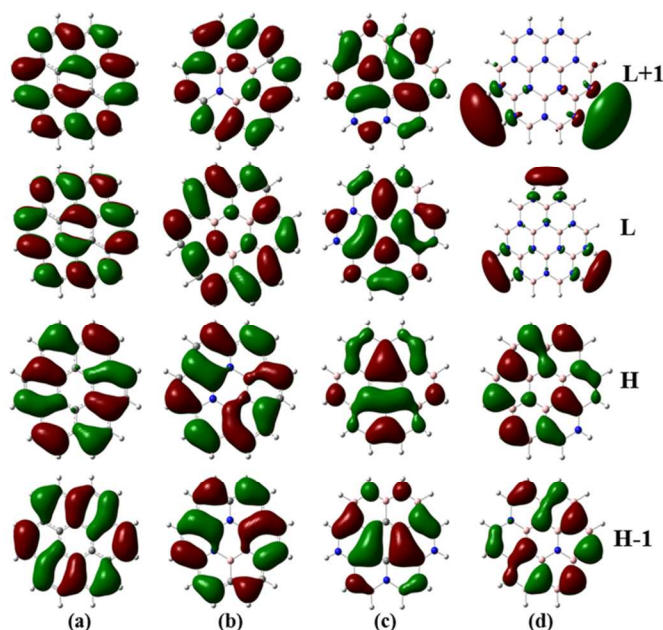


**Figure 2:** Isosurfaces of frontier molecular orbitals (FMOs) calculated for the pristine coronene (a), mid-BN-coronene (b), peri-BN-coronene (c), and full-BN-coronene (d) monomers.

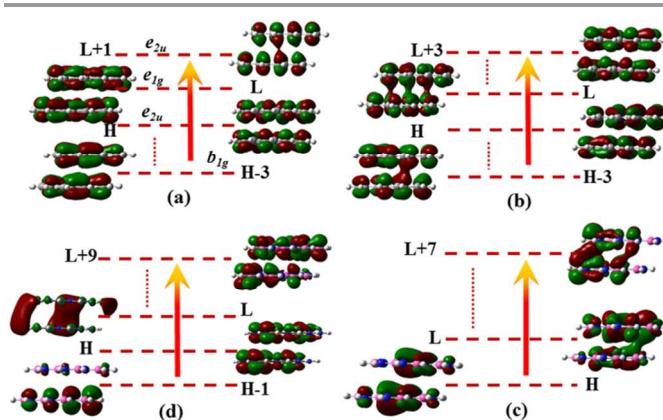


**Figure 3:** (Clockwise from Top Left) Molecular orbital diagrams showing the lowest energy transition of highest probability (large oscillator strength) for the dimeric stacks of coronene (a), mid-BN-coronene (b), peri-BN-coronene (c) and full-BN-coronene (d).

Furthermore, to understand the influence of  $\pi$ - $\pi$  and electrostatic interactions on the excited state properties of these dimer stacks, we perform TDDFT calculations for the dimer geometries using B3LYP/6-31+G(d,p). We consider the optimized geometry obtained using the dispersion corrected density functional  $\omega$ B97XD, that corresponds to the most stable slip-stacked (AB) structure of pristine coronene and its BN substituted analogues. We calculate the low-energy excitations which correspond to the large oscillator strength (i.e., strong absorbing states). For analysing the nature of electronic excitations, we also look at the most important orbital transitions. All results are provided in Table 3. We find that the low-energy excitations are slightly blue-shifted (higher energy) compared to the monomer's excitations. This is because of slightly reduced orbital interactions due to the small structural distortion in the stacked dimer geometries compared to the monomer's FMOs distribution (see Fig. 3). The results show that the low energy optical absorption with large oscillator strength occurs due to electrons getting mainly promoted from the core occupied molecular orbital (OMO) to comparatively higher energy unoccupied molecular orbital (UMO) (see Table 3).

### 3.2. Bulk Electronic and Charge Transport Properties of Various BN-Coronene Crystals:

To understand the bulk properties of various BN-substituted coronene systems considered, we have investigated the electronic structure of different BN-modified crystals, which all are modelled from the pristine coronene crystal structure. The modeled crystal structures are fully optimized using dispersion corrected DFT employing GGA-PBE exchange-correlation functional<sup>56</sup> with projected augmented plane wave (PAW<sup>57, 58</sup>) basis as implemented in VASP<sup>45, 46</sup> code. Plane wave energy cut off of 400 eV is used for all calculations. For structural relaxations, we have used  $3 \times 3 \times 3$  Monkhorst-pack k-grid mesh and the single point calculations are carried out using  $5 \times 5 \times 5$  k-grid mesh for sampling 3D Brillouin zone. Geometry

optimization using  $5 \times 5 \times 5$  k-grid mesh for pristine coronene crystal is performed in order to ensure the structural and energy convergences. Total energy difference between the two optimized structures is found to be small (a few meV only).

For the crystal structure of coronene, we have considered the structure reported by Fawcett *et al.* in 1966.<sup>29</sup> It has a monoclinic structure having space group  $P2_1/a$ , with  $a = 16.119$ ,  $b = 4.702$ ,  $c = 10.102$ ,  $\alpha = 90.00$ ,  $\beta = 110.90$  and  $\gamma = 90.00$ . Unit cell contains 2 coronene molecules, consisting of total 72 atoms. Here, we first analyse and compare the changes in optimized modelled unit cell parameters of various BN-substituted coronene crystal considered. We find slight changes in the structural parameters (important bond lengths and inter-planar distance) of coronene molecule present in crystal geometry than DFT optimized geometry. All the average C-C and B-N bond distances along with the stacking distance of all five systems are listed in Table 6. However, for calculations of transport properties of these systems, we have considered both the crystal structures ( $P2_1/a$  space group) as well as the dispersion corrected DFT (VASP) optimized structures.

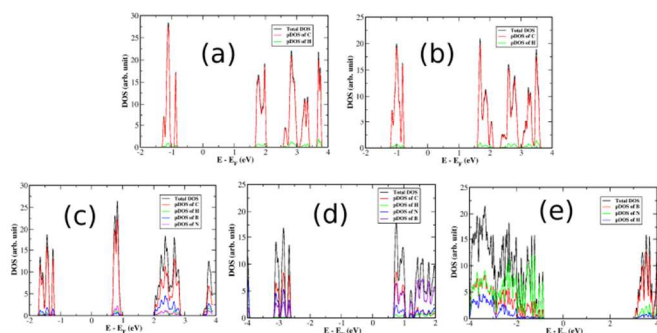


**Figure 4:** The electronic DOS and pDOS calculated for the coronene crystal unit cell (a), and DFT optimized unit cell of pristine coronene (b), mid-BN-coronene (c), peri-BN-coronene (d) and full-BN-coronene (e). (All calculations are carried out using dispersion corrected DFT employing GGA-PBE exchange-correlation functional as implemented in VASP code)

Structural optimizations using dispersion corrected DFT show that there is an increase in inter-planar stacking distances by  $0.15 \text{ \AA}$  for the pristine coronene when compared to the crystal geometry. The difference is due to the slight changes in crystal parameters upon geometry optimizations. Note that, the coronene crystallization was carried out at room temperature (i.e., at 300 K), while the DFT optimization is performed at 0 K temperature. This may cause slight differences in structural parameters. We also find slight changes in average C-C and B-N bond distances from the crystal geometry (see Table 4).

### 3.2.1. Bulk Electronic Structures:

The calculated band gap values together with the electronic density of states (DOS) and projected density of states (pDOS) are analyzed for understating the bulk electronic properties of these systems. The results show that band-gap increases with increase in BN concentration, which is also in accordance with the results on a larger h-GNF as will be discussed in section 3.3

and corroborated with the result reported by Xu *et al.*<sup>59</sup> The calculated electronic band gaps follow the order: mid-BN-coronene (1.88 eV) < pristine coronene (2.30 eV) < peri-BN-coronene (3.23 eV) < full-BN-coronene (4.15 eV). We find relatively small band gap (1.88 eV) calculated for the mid-BN-coronene crystal (see Table 6). Note that, the band gap of pristine coronene crystal (without geometry optimization) is found to be 2.63 eV, which is very close to the optical band gap of 2.8 eV predicted by experimental fluorescence emission study from electron energy loss spectroscopy (EELS).<sup>60</sup> Slight under estimation of electronic band gap is due to lack of quasi-particle behaviour and electron self-interaction errors within the DFT methods employed here.

In order to understand the variation in band-gap, the electronic density of states (DOS) and its projection on individual species, i.e., projected density of states (pDOS) are calculated with increasing concentration of BN ranging from 0% to 100% (i.e., for four structures studied) and are shown in Fig. 4. The pDOS shows that the top of valence band and bottom of the conduction bands mainly consist of C  $p_z$  orbitals for the three model coronene crystals, except for the full-BN-coronene, for which we find completely localized valence and conduction bands arising from the N and B  $p_z$  orbitals, respectively. The results also show that the valence electronic states are partially composed of N  $p_z$  orbitals, while the B  $p_z$  orbitals dominates the conduction bands nature (see Fig. 4). This suppresses the  $\pi$ -electrons delocalization for the BN-modified crystals and thus, increases the band-gap. The changes in band-gap can be accounted for the changes in electron localization with varying B-N concentrations and its position.<sup>61</sup>

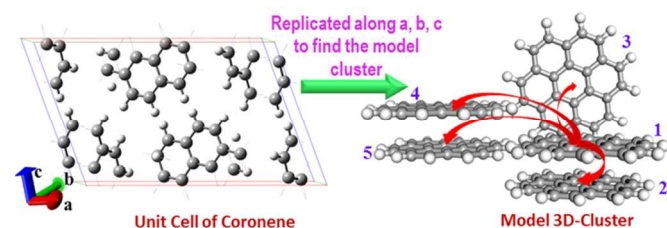


**Figure 5:** (Left) Unit cell of coronene containing 2 molecules; (Right) Model 3-dimensional cluster of coronene and other modeled systems taken for charge transfer hopping study.

### 3.2.2. Charge Transport Characteristics:

Coronene molecule possesses extended  $\pi$ -conjugation and thus expected to show high charge transport characteristics. In fact, most aromatic molecules exhibit this trend. For the microscopic perception of charge transport behaviour, it is important to gain an idea about the hopping matrix elements/effective charge transfer integral ( $J_{eff}$ ) and reorganization energy ( $\lambda$ ), the two intrinsic parameters that govern the overall charge transport through a crystal. These parameters provide an impression whether a crystal would act as an electron or hole transporter. These parameters have been calculated here according to the mathematical equations given in Supporting Information.

As has been discussed above, both pristine coronene and mid-BN-coronene exhibit similar electronic properties. This is also reflected in the calculated reorganization energy values (see in Table 6). The  $\lambda$  computed here considers only the inner-sphere part neglecting the outer-sphere contribution. The results show similar trend of possessing higher  $\lambda_{elec}$  than  $\lambda_{hole}$ . On the other hand, full-BN-coronene and peri-BN-coronene show similar nature, exhibiting larger  $\lambda_{hole}$ . This clearly indicates the differences in charge transport behaviours. The former two are expected to have large hole mobility, while electron mobility is expected to be dominant for the latter two crystals. Surprisingly, as listed in Table 4,  $\lambda_{elec}$  is found to be very small (by an order of magnitude) than  $\lambda_{hole}$  in case of full-BN-coronene. This suggests significantly large electron mobility for this crystal. To understand the exchange and correlation functional dependence of reorganization energy, we have repeated the calculations for full-BN-coronene using two other energy functionals, namely meta-GGA functional M062X and the Local Spin Density Approximation (LSDA), that uses Slater exchange functional and the Vosko, Wilk, and Nusair 1980 correlation functional (VWN). The results show similar trend in reorganization energy ( $\lambda_{hole} > \lambda_{elec}$ ) obtained for full-BN-coronene using different energy functional (see Table S1). An analysis of charge density differences and the ESP iso-surfaces (see Fig. S1) calculated for the neutral and charge species (cation and anion) reveal that the excess charges are mainly distributed among the electron deficient B atoms present in full-BN-coronene.

Additionally, charge transfer integrals (i.e., the hopping matrix element) ( $J_{eff}$ ) are important for discerning the microscopic nature of charge transport in these  $\pi$ -conjugated materials and thus, holds relevance too in understanding their hole or electron transport nature. In general, charge transport mechanism involves transfer of charge carriers (electron or hole) from a charged species to an adjacent neutral molecule and thereby, directly related to the  $J_{eff}$ .

Here, we have calculated all possible  $J_{eff}$  for the cluster model shown in Fig. 5. All  $J_{eff}$  values calculated at the different centre of mass distances are listed in Table S2. For the nearest neighbour  $\pi$ -stacked dimers, we find considerably high  $J_{eff}^{hole}$  for coronene, mid-BN-coronene and peri-BN-coronene. Contrastingly, the  $J_{eff}^{elec}$  is found to be large for the full-BN-coronene than the  $J_{eff}^{hole}$ . Thus, we find that with full B-N substitution for all the C-C bonds in coronene alters the nature of predominant hopping integral. This is because of decreased  $\pi$ - $\pi$  interactions and in turn, reduced electronic delocalization for the full-BN-coronene. The enhanced electrostatic interactions between the two AB  $\pi$ -stacked layers are also responsible for the larger  $J_{eff}^{elec}$ .

Next we look at the carriers mobilities calculated for these crystals. The charge carrier mobility computed using semi-classical Marcus formalism shows that coronene is a hole transporter, as was reported in our earlier work<sup>32</sup> too. Introduction of a h-BN ring at the center, i.e., for mid-BN-

coronene, results in large hole mobility compared to value found for the pristine coronene. This can be ascribed due to the enhanced  $\pi$ -electrons delocalization at the peripheral rings, which helps hopping of charge carrier (hole) to the neighboring molecules within the crystal. On the contrary, substitution of the peripheral ring C atoms by BN in coronene (i.e., peri-BN-coronene) increases the electron mobility of the system. For fully substituted BN-coronene system, the calculations show the electron mobility to be very high of about 27.89 cm<sup>2</sup>/Vs than the hole mobility. To understand this unexpectedly high electron mobility value found for full-BN-coronene, we carefully look at the two intrinsic energetic parameters (reorganization energy and hopping strength) that govern the overall charge carriers' mobilities within Marcus approach. We find very small electron reorganization energy which results in large mobility value (see Table 4 and S1). The main point is that, within semi-classical Marcus Theory and with varying the functionals, we find full-BN-coronene shows large electron mobility and small hole mobility. We would expect these results could be verified experimentally for the bigger graphene nanoflakes too by methodical substitution of C-C by B-N.

**Table 4:** Inter-planar stacking distances, electronic band gap, reorganization energy and charge carrier mobility for the crystals that are obtained from the periodic calculations using VASP code.

System	Inter-planar distance (Å)	Avg. C-C (Å)	Avg. B-N (Å)	Calculated Band gap (eV)	Reorganization Energy, $\lambda$ (eV)		Mobility (cm <sup>2</sup> V <sup>-1</sup> s <sup>-1</sup> )	
					Electron	Hole	Electron	Hole
coronene (crystal)	3.50	1.40	-	2.63	0.1724	0.1294	0.16	2.46
coronene (optimised)	3.65	1.41	-	2.30	0.1673	0.1266	0.97	3.91
mid-BN-coronene	3.63	1.40	1.44	1.88	0.1591	0.1244	0.35	2.99
peri-BN-coronene	3.58	1.41	1.43	3.23	0.2392	0.3564	0.19	0.19
full-BN-coronene	3.51	-	1.38	4.15	0.0120	0.1403	27.89	1.18

### 3.3. Optical properties of a large hexagonal graphene nanoflake with varying concentration of BN substituent:

So far, we have seen that the topological nature of BN substituents in coronene results in diverse opto-electronic properties. The electronic structure and optical properties of h-GNFs are expected to be altered when subjected to varying extent of BN-substitution. Moreover, the properties may evolve differently with systems sizes. Theoretically, it has already been shown that the second hyperpolarizability can be significantly large for different GNF sizes, which makes it important in non-linear optical study.<sup>62</sup>

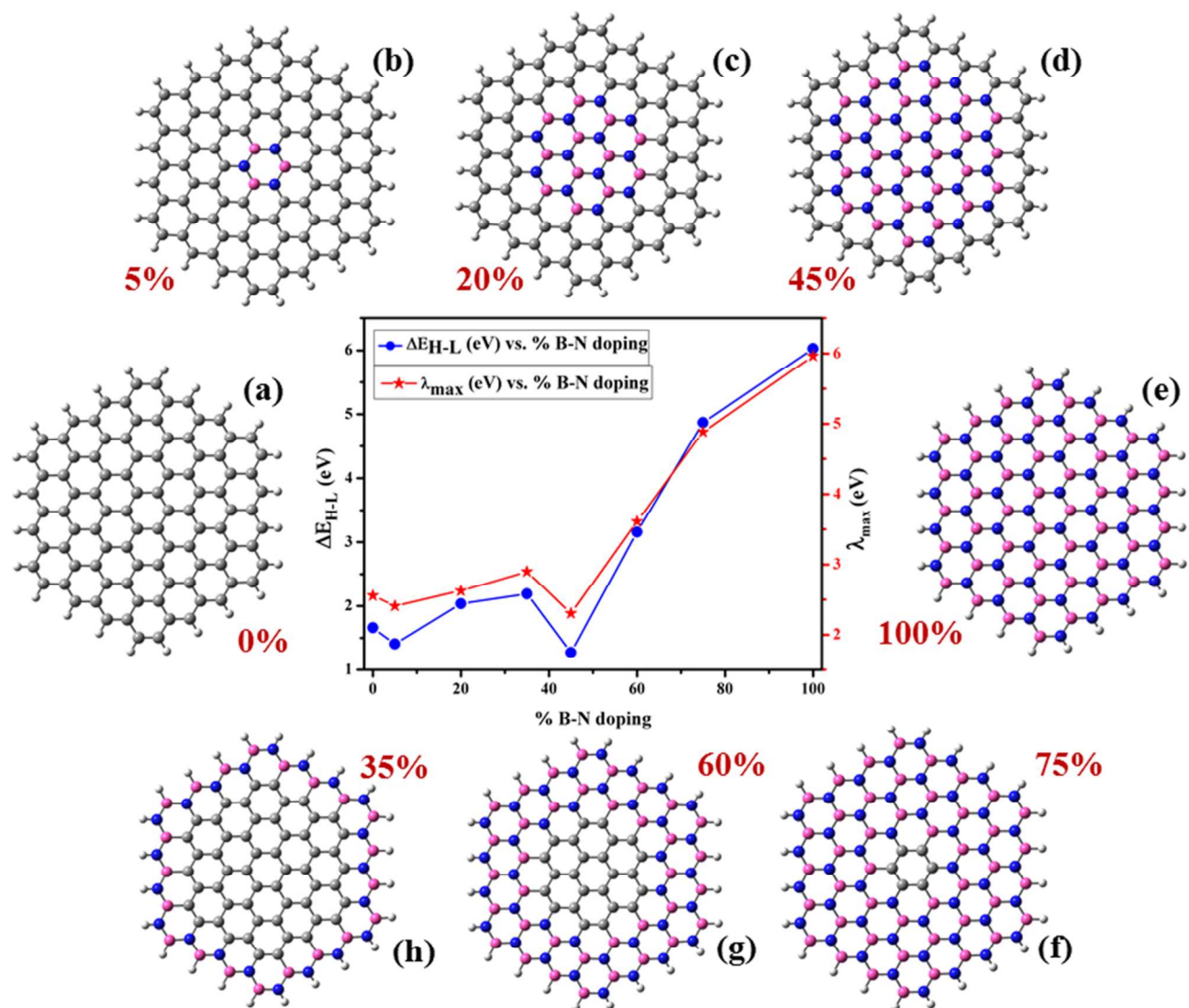


Figure 6. Optimized structures and plot showing the relationship between %B-N substitution with  $\lambda_{max}$  and  $\Delta E_{H-L}$ .

It would be interesting to examine the effects of different BN substituents and its concentrations on a larger size h-GNF's optical properties. This may have possible applications in light-emitting devices. Here, we have studied the changes in optical properties by performing excited state TDDFT calculations for the larger sizes zigzag edge h-GNFs subjected to different BN substitutions. To this end, we consider a large h-GNF consisting of 120 atoms and substitute the C-C pairs systematically with the B-N pairs. We begin with pristine h-GNF [(a), in Fig. 6] and replace the core hexagonal CC rings by different sizes h-BN rings with increasing the h-BN domain

sizes towards periphery [(b), (c), (d) and (e) in Fig. 6]. We also consider replacing the core h-BN rings in (e) with varying sizes h-CC rings to create structures (f), (g) and (h) (see in Fig. 6). Thus, we have considered eight systems in total and each of them possesses different BN content. All excited states results (excitation energy, oscillator strength and HOMO-LUMO gap) are given in Table S3. A diagram is also shown in Fig. 6 for displaying the BN concentration dependence of calculated low-energy optical absorption (corresponding to the large oscillator strength) and electronic HOMO-LUMO gap values.

As can be seen from Fig. 6 and Table S3, we find a red-shift in the optical absorption with increase in BN concentrations of about 5% in the h-GNF, and this also agrees well with the variation of the electronic-gap ( $\Delta E_{H-L}$ ). Further BN substitution up to 35% causes increased excitations energy and large  $\Delta E_{H-L}$  gap values, indicating blue-shift in the linear absorption spectra. Interestingly, a large red-shift and small electronic gap are predicted at the 45% BN substituent concentration. At this BN concentration (45%) the modified h-GNF system [(d), in Fig. 6] resemblances to the system of mid-BN-coronene, where we found very small  $\Delta E_{H-L}$  gap and red-shift in the optical absorption due to the enhanced  $\pi$ -delocalization effects at the peripheral C-C rings. After this critical BN concentration, we find systematic blue-shift in low-energy excitations up to the maximum substituent concentrations (i.e., 100%). A large BN content (i.e., less CC/BN ratio) in h-GNF creates localized states by suppressing the  $\pi$ -electrons delocalization. Therefore, it leads to the observed blue-shift in optical absorption and large electronic  $\Delta E_{H-L}$  gap. The results predicted here for large h-GNFs are fully consistent with the findings discussed above in the context of coronene (small h-GNF). Here, we found that the nature and concentrations of BN substituent play an important role in tuning electronic structure and optical property of modified h-GNFs. In addition, since the calculated optical properties span over a wide range of wavelengths in the UV-visible spectrum, they may find potential in optical nano-devices applications and photo-catalysts.

### Conclusions:

In summary, we have investigated the structural stability and opto-electronic properties of various BN substituted h-GNFs to explore and understand their plausible improved device functionality. Coronene, a smallest h-GNF, is considered at first place and analyzed the different structure-property responses when subjected to various iso-electronic BN substitutions for the CC bonds. The results suggest tunable opto-electronic and charge transport properties depending on the topological position of BN substituent and its concentrations. The results show a systematic trend in calculated charge carrier's mobilities with increasing BN content. We report very high hole mobility for the pristine and mid-BN coronene, while the electron mobility value is found to be very large for full-BN-coronene. We have also examined the effects of varying BN concentrations on the opto-electronic properties of larger sizes h-GNFs and shown their potential in optical devices. Moreover, it is found that the bulk electronic and charge transport properties of different BN substituted coronene crystals mainly depends on the nature of BN substitution and its concentrations. The microscopic understanding for the tunable properties is also provided in detail. The study suggests diverse opto-electronic and charge transport properties depending on hierarchy of BN substitutions in h-GNFs for designing advanced device applications.

### Acknowledgements:

SS acknowledges JNCASR for financial assistance, AKM acknowledges CSIR, Govt. of India for senior research fellowship and SKP acknowledges DST, Govt. of India for funding.

Electronic Supplementary Information (ESI) available: Electrostatic Potential Plots, Distance dependent charge transfer integrals of model 3D cluster and Optical Data for hexagonal GNF. See DOI: 10.1039/b000000x/

### Notes and references

<sup>a</sup>Theoretical Sciences Unit, Jawaharlal Nehru Centre for Advanced Scientific Research, Bangalore, 560064, India. E-mail: pati@jncasr.ac.in; Fax: +91-80-22082766/2767; Tel: +91-80-22082839/2575, <sup>b</sup>New Chemistry Unit, Jawaharlal Nehru Centre for Advanced Scientific Research, Bangalore, 560064, India. E-mail: pati@jncasr.ac.in; Fax: +91-80-22082766/2767; Tel: +91-80-22082839/2575

1. J. E. Anthony, *Chem. Rev.*, 2006, **106**, 5028-5048.
2. A. L. Appleton, S. M. Brombosz, S. Barlow, J. S. Sears, J. L. Bredas, S. R. Marder and U. H. Bunz, *Nat. Commun.*, 2010, **1**, 91.
3. H. Angliker, E. Rommel and J. Wirz, *Chem. Phys. Lett.*, 1982, **87**, 208-212.
4. H. Yamagata, J. Norton, E. Hontz, Y. Olivier, D. Beljonne, J. L. Bredas, R. J. Silbey and F. C. Spano, *J. Chem. Phys.*, 2011, **134**, 204703-204711.
5. T. M. Halasinski, D. M. Hudgins, F. Salama, L. J. Allamandola and T. Bally, *J. Phys. Chem. A*, 2000, **104**, 7484-7491.
6. C. Raghu, Y. Anusooya Pati and S. Ramasesha, *Phys. Rev. B*, 2002, **66**, 035116.
7. M. Slawik and P. Petelenz, *J. Chem. Phys.*, 1999, **111**, 7576-7582.
8. R. Rieger and K. Müllen, *J. Phys. Org. Chem.*, 2010, **23**, 315-325.
9. F. R; and E. M, *Bull. Chem. Soc. Jpn.*, 2013, **86(4)**, 445-451.
10. Y. H. Kim, S. H. Kwon, J. M. Lee, M. S. Hwang, J. H. Kang, W. I. Park and H. G. Park, *Nat. Commun.*, 2012, **3**, 1123.
11. X. Du, I. Skachko, A. Barker and E. Y. Andrei, *Nat Nano*, 2008, **3**, 491-495.
12. M. J. D. Bosdet and W. E. Piers, *Can. J. Chem.*, 2009, **87**, 8-29.
13. Y. Lu, A. Bolag, J.-i. Nishida and Y. Yamashita, *Synth. Met.*, 2010, **160**, 1884-1891.
14. P. Wang and C. Zhang, *J. Mol. Struct. THEOCHEM*, 2010, **955**, 84-90.
15. A. J. Ashe and Fang, *Org. Lett.*, 2000, **2**, 2089-2091.
16. P. G. Campbell, E. R. Abbey, D. Neiner, D. J. Grant, D. A. Dixon and S.-Y. Liu, *J. Am. Chem. Soc.*, 2010, **132**, 18048-18050.
17. A. M. van de Craats, N. Stutzmann, O. Bunk, M. M. Nielsen, M. Watson, K. Müllen, H. D. Chanzy, H. Siringhaus and R. H. Friend, *Adv. Mater.*, 2003, **15**, 495-499.

18. S. Xiao, J. Tang, T. Beetz, X. Guo, N. Tremblay, T. Siegrist, Y. Zhu, M. Steigerwald and C. Nuckolls, *J. Am. Chem. Soc.*, 2006, **128**, 10700-10701.
19. U. Rohr, P. Schlichting, A. Böhm, M. Gross, K. Meerholz, C. Bräuchle and K. Müllen, *Angew. Chem. Int. Ed.*, 1998, **37**, 1434-1437.
20. V. Casagrande, A. Alvino, A. Bianco, G. Ortaggi and M. Franceschin, *J. Mass Spectrom.*, 2009, **44**, 530-540.
21. R. Rieger, M. Kastler, V. Enkelmann and K. Müllen, *Chem. Eur. J.*, 2008, **14**, 6322-6325.
22. S. S. Naghavi, T. Gruhn, V. Alijani, G. H. Fecher, C. Felser, K. Medjanik, D. Kutnyakhov, S. A. Nepijko, G. Schönhense, R. Rieger, M. Baumgarten and K. Müllen, *J. Mol. Spectrosc.*, 2011, **265**, 95-101.
23. C. A. Jaska, D. J. H. Emslie, M. J. D. Bosdet, W. E. Piers, T. S. Sorensen and M. Parvez, *J. Am. Chem. Soc.*, 2006, **128**, 10885-10896.
24. E. R. Abbey, L. N. Zakharov and S.-Y. Liu, *J. Am. Chem. Soc.*, 2011, **133**, 11508-11511.
25. C. Tönshoff, M. Müller, T. Kar, F. Latteyer, T. Chassé, K. Eichele and H. F. Bettinger, *ChemPhysChem*, 2012, **13**, 1173-1181.
26. M. J. D. Bosdet, W. E. Piers, T. S. Sorensen and M. Parvez, *Angew. Chem. Int. Ed.*, 2007, **46**, 4940-4943.
27. D. Ghosh, G. Periyasamy and S. K. Pati, *Phys. Chem. Chem. Phys.*, 2011, **13**, 20627-20636.
28. T.-L. Chiu, W.-F. Xu, C.-F. Lin, J.-H. Lee, C.-C. Chao and M.-K. Leung, *Appl. Phys. Lett.*, 2009, **94**, 013307-013303.
29. J. K. Fawcett and J. Trotter, *Proc. R. Soc. Lond. A*, 1966, **289**, 366-376.
30. J. Oomens, B. G. Sartakov, A. G. G. M. Tielens, G. Meijer and G. v. Helden, *ApJ*, 2001, **560**, L99.
31. H. Morris and J. Yates, *Discuss. Faraday Soc.*, 1971, **51**, 24-36.
32. S. Sanyal, A. K. Manna and S. K. Pati, *J. Phys. Chem. C*, 2012, **117**, 825-836.
33. J. Wu, W. Pisula and K. Müllen, *Chem. Rev.*, 2007, **107**, 718-747.
34. A. M. Silva, M. S. Pires, V. N. Freire, E. L. Albuquerque, D. L. Azevedo and E. W. S. Caetano, *J. Phys. Chem. C*, 2010, **114**, 17472-17485.
35. K. P. Loh, Q. Bao, P. K. Ang and J. Yang, *J. Mater. Chem.*, 2010, **20**, 2277-2289.
36. A. K. Manna and S. K. Pati, *J. Phys. Chem. C*, 2011, **115**, 10842-10850.
37. L. Türker, *Polycyclic Aromat. Compd.*, 2012, **32**, 61-74.
38. M. Kayanuma, T. Ikeshoji and H. Ogawa, *Bull. Chem. Soc. Jpn.*, 2011, **84**, 52-57.
39. M. Winkler and K. N. Houk, *J. Am. Chem. Soc.*, 2007, **129**, 1805-1815.
40. S. Giri, A. Chakraborty and P. K. Chattaraj, *Stability and aromaticity of nH<sub>2</sub>@B<sub>12</sub>N<sub>12</sub> (n = 1-12) clusters*, 2011.
41. Y. Zhao, X. Wu, J. Yang and X. C. Zeng, *Phys Chem Chem Phys*, 2012, **14**, 5545-5550.
42. M. J. Frisch, G. W. Trucks, H. B. Schlegel, G. E. Scuseria, J. R. C. M. A. Robb, G. Scalmani, V. Barone, B. Mennucci, H. N. G. A. Petersson, M. Caricato, X. Li, H. P. Hratchian, J. B. A. F. Izmaylov, G. Zheng, J. L. Sonnenberg, M. Hada, K. T. M. Ehara, R. Fukuda, J. Hasegawa, M. Ishida, T. Nakajima, O. K. Y. Honda, H. Nakai, T. Vreven, J. A. Montgomery, Jr., F. O. J. E. Peralta, M. Bearpark, J. J. Heyd, E. Brothers, V. N. S. K. N. Kudin, R. Kobayashi, J. Normand, A. R. K. Raghavachari, J. C. Burant, S. S. Iyengar, J. Tomasi, N. R. M. Cossi, J. M. Millam, M. Klene, J. E. Knox, J. B. Cross, C. A. V. Bakken, J. Jaramillo, R. Gomperts, R. E. Stratmann, A. J. A. O. Yazyev, R. Cammi, C. Pomelli, J. W. Ochterski, K. M. R. L. Martin, V. G. Zakrzewski, G. A. Voth, J. J. D. P. Salvador, S. Dapprich, A. D. Daniels, J. B. F. O. Farkas, J. V. Ortiz, J. Cioslowski, and G. and D. J. Fox, Inc., Wallingford CT., in *Gaussian 09, Revision A.02*, 2009.
43. A. D. Becke, *Phys. Rev. A*, 1988, **38**, 3098-3100.
44. P. J. Stephens, F. J. Devlin, C. F. Chabalowski and M. J. Frisch, *J. Phys. Chem.*, 1994, **98**, 11623-11627.
45. G. Kresse and J. Furthmüller, *Phys. Rev. B*, 1996, **54**, 11169-11186.
46. G. Kresse and J. Furthmüller, *Comput. Mater. Sci.*, 1996, **6**, 15-50.
47. G. te Velde, F. M. Bickelhaupt, E. J. Baerends, C. Fonseca Guerra, S. J. A. van Gisbergen, J. G. Snijders and T. Ziegler, *J. Comput. Chem.*, 2001, **22**, 931-967.
48. K. Burke, J. P. Perdew and M. Ernzerhof, *Int. J. Quantum Chem*, 1997, **61**, 287-293.
49. W. Shen, M. Li, Y. Li and S. Wang, *Inorg. Chim. Acta*, 2007, **360**, 619-624.
50. R. Islas, E. Chamorro, J. Robles, T. Heine, J. Santos and G. Merino, *Struct. Chem.*, 2007, **18**, 833-839.
51. T. Heine, R. Islas and G. Merino, *J. Comput. Chem.*, 2007, **28**, 302-309.
52. R. B. King, *J. Math. Chem.*, 1990, **4**, 69-85.
53. S. F. Boys and F. Bernardi, *Mol. Phys.*, 1970, **19**, 553-566.
54. S. Simon, M. Duran and J. J. Dannenberg, *J. Chem. Phys.*, 1996, **105**, 11024-11031.
55. R. M. Minyaev, V. I. Minkin, T. N. Gribanova, A. G. Starikov and R. Hoffmann, *J. Org. Chem.*, 2003, **68**, 8588-8594.
56. G. K. H. Madsen, *Phys. Rev. B*, 2007, **75**, 195108.
57. P. E. Blöchl, *Phys. Rev. B*, 1994, **50**, 17953-17979.
58. G. Kresse and D. Joubert, *Phys. Rev. B*, 1999, **59**, 1758-1775.
59. B. Xu, Y. H. Lu, Y. P. Feng and J. Y. Lin, *J. Appl. Phys.*, 2010, **108**, -.
60. F. Roth, J. Bauer, B. Mahns, B. Büchner and M. Knupfer, *Phys. Rev. B*, 2012, **85**, 014513.
61. Q. Peng and S. De, *Physica E: Low-dimensional Systems and Nanostructures*, 2012, **44**, 1662-1666.
62. H. Nagai, M. Nakano, K. Yoneda, R. Kishi, H. Takahashi, A. Shimizu, T. Kubo, K. Kamada, K. Ohta, E. Botek and B. Champagne, *Chem. Phys. Lett.*, 2010, **489**, 212-218.

**Graphical Abstract for Manuscript Id: TC-ART-12-2013-032486****Title: BN-Decorated Graphene Nanoflakes for Tunable Opto-electronic and Charge Transport Properties**